Ultrafast Dynamics of Nanoparticles
in Highly Intense X-Ray Pulses

vorgelegt von

M. Sc.

Maximilian Jakob Bucher

geb. in Frankfurt am Main

von der Fakultät II - Mathematik und Naturwissenschaften
der Technischen Universität Berlin
zur Erlangung des akademischen Grades

Doktor der Naturwissenschaften
- Dr. rer. nat. -

genehmigte Dissertation

Promotionsausschuss:

Vorsitzender: Prof. Dr. Mario Dähne
Berichter/Gutachter: Prof. Dr. Thomas Möller
Berichter/Gutachter: Prof. Dr. Christoph Bostedt

Tag der wissenschaftlichen Aussprache: 24. Dezember 2016

Berlin 2016

M.Sc. Maximilian Jakob Bucher

Argonne National Laboratory

Chemical Sciences and Engineering Division

Argonne, IL 60439, USA

E-Mail: buchermj@anl.gov

Web: https://www.max-bucher.de

Abstract

abstract text here

Kurzfassung

deutsche Kurzfassung hier

Contents

Contents

List of Figures

List of Tables

1 Introduction

Investigating matter with light is one of the most fundamental approaches to study nature. Whether we look at things by eye or use more advanced methods for example using lasers, it is an invaluable tool to understand nature. Through light, we can study the shapes of objects, investigate fundamental particles, study quantum mechanics and so much more. Key aspect in almost any study involving light is it's wavelength. The wavelength of light can make you feel cozy at home with a modern LED light bulb or shroud your home in a blue, uncomfortable haze when you use older light bulbs. At the end of the 19th century, Röntgen discovered the then novel X-radiation and quickly realized its impact due to its different wavelength. Soon, he was able to take first medical X-ray images, later X-rays could be used to investigate fundamental aspects of atoms. The success story continues until today, where short wavelength X-rays enables the study of the workhorse in human bodies, namely proteins. The shape of a protein, which is only a few nanometers in size, cannot be seen in a microscope anymore and only X-rays can be used to unravel their shape with sufficient resolution. The shape of a biomolecules is of particular interest because it defines its biological function. The chemical structure of most human biomolecules are fairly similar and affect the function little. Medical drugs often aim to affect biological functions such that the specific shape of a protein becomes very important for drug research and drug design.

However, there is more to light than just its wavelength. The intensity of light plays a crucial role, for example when we are sitting in front of a fire and the warm glaze of infrared (IR) radiation can be felt on our skin. Anyway, using high intense radiation allows us to create an environment comparable to the inside of the sun, where fusion processes create energy and other interesting high energy processes are happening. Intense light is also needed if you want to study the very small because the interaction between matter and light becomes very small on length scales of for example a protein. To study the shape of a protein a certain interaction is needed and since we do not want to change the protein, we have to adjust the intensity of light.

Last but not least, light can come in short flashes for example when taking a photograph. At night, when the flash is too long, the pictures often get washed out. It is

similar when you study nature, if you want to look at some movement or more general dynamics, your light flash must be short enough to resolve this dynamic, otherwise it gets washed out. Proteins function also through movement. Many of their dynamics could already be deciphered but it is unclear what one would discover if one would look at even faster timescales.

Summarizing, a light flash can be described by by its wavelength, intensity and duration. To study matter, e.g. proteins, one has to optimize these three parameters a lot. TTherefore, a new kind of light source was developed that is particularly interesting for imaging the very small on the nanometer scale. The first one of these light sources, a so called free electron laser (FEL), was build in Hamburg, Germany. First experiments with FELs that showed proof of principle studies showcasing capabilities of FELs as a highly intense and ultra short light pulse source. As a result, more advanced X-ray free electron laser (XFEL) were built to further improve capabilities. The first hard XFEL was built in Menlo Park, California at Stanford University and is called the Linac Coherent Light Source (LCLS). It is a 4.1 km long machine[1], the most straightest building in the world[2], is build underneath the ground and the interstate I-280 crosses it via a bridge[3]. This massive machine delivers what is needed to use imaging techniques that have been out of reach so far. To name a few, with LCLS it is possible to study protein crystals of much smaller size, one can study single particles for example viruses and cells. And LCLS is not limited to imaging techniques, one can study atoms and molecules in thus far unreachable regimes and also understand magnetism better. The reason these new areas of study area accessible through LCLS lay in the light parameters. LCLS produces light with a very short wavelength (X-rays from 4.6 nm to 0.1 nm), it has a very high intensity ($10^18 Ws/cm^2$) and ultra short pulses ($1 - 500 fs$). The combination of these parameters is unique in the world and enables us to look at things that have been hidden so far.

Let us now imagine that we expose a protein to the very intense X-rays from LCLS (or any other XFEL). Within the first moment of interaction from the light and the proteins, the protein scatters photons distinctive to it shape that we are able measure and hence recover the shape of the protein. But the protein will also absorb the light and therefore energy and will become very hot, much like the conditions on the surface of the sun. The hot protein will expand quickly and disintegrate into its atomic components. While

---

[1]Measurement on Google maps from the injector building to the far experimental hall.

[2]The European XFEL in Hamburg, Germany is currently build to similar engineering requirements.

[3]On a fun note, the accelerator part of LCLS is actually older than the I-280 and do avoid interruptions of the experiments, the bridge was build long before the intersate and there are pictures of this bridge that is not connected to any streets.

the scattering process is desired the inevitable absorption process will ultimately hinder the scattering process and limit the resolution of our measurement. The damage that occurs to the sample is an ultra-fast process that can only be studied with an even faster light pulse. It is a process that thus far is known to exist but has been hidden due to the limitation of other light sources. XFEL offer now the opportunity to study this process that is applicable to a variety of X-ray imaging techniques ranging from crystallography to spectroscopic applications over to the imaging of single particles.

This thesis discusses an experiment performed with LCLS to study the effects and dynamics induced by radiation damage on homogenous xenon and helium clusters and heterogeneous clusters consistent of xenon and helium. A detailed and time-resolved X-ray pump – X-ray probe study is undertaken to first induce X-ray related dynamics via a X-ray pump pulse and then create a single-shot image of the cluster at a given time delay. We combine the single particle imaging technique with a time-of-flight mass spectrometer that yields insights into ionization dynamics, absorbed energies and particle heterogeneity. Rare gas clusters are used as sample target as they are an ideal nanosamples in the gas phase. They are easy to produce and easy to transport to the interaction region with LCLS. Furthermore they can be tuned in size and multiple rare gases, here xenon and helium, can be combined to form a single nanometer sized heterogeneous cluster. We present the data from the study in form of real space images from clusters complemented by diffraction images. Furthermore, we correlate the time-of-flight data to each image.

The thesis is organized as follows, chapter 2 discusses fundamental aspects and background information to the performed studies. Chapter 3 focuses on the experimental setup of this study, chapter 5 presents the results obtained and finally 6 sumarises the previous chapters and provides an outlook for further studies.

2 Fundamental Concepts

This chapter tries to condense some of the theoretic basics that will reoccur throughout the thesis. We start off with an introduction to the key aspects of X-ray free electron lasers including the more specific parts of self-seeding and X-ray pump – X-ray probe techniques, followed by a section about the formation of rare gas clusters. We then dive into the interaction of light and matter, starting with X-ray scattering including the broad topic of phase retrieval in diffraction patterns and ending with the ionization of matter and formation of a nanoplasma.

2.1 X-ray free electron laser

The advance of X-ray free electron laser in the recent years has enabled experimental ideas from long ago but has also opened entirely new branches to research. Thus far synchrotron radiation facilities have provided X-rays to a great variety of communities but the pulse characteristics of the synchrotron storage rings are limited. A synchrotron accelerates a number of electron bunches near the speed of light and then injects them into a storage ring at which point the electron bunches can be little manipulated and loose energy as they circle around the ring and create photons. As a result, synchrotron sources are limited in their spectral brightness, which we can define as

$$B = \frac{n}{A \; \Theta \; t \; \Delta E},$$

(2.1)

with n being the number of photons, A the unit source size, Θ the divergence of the beam, t the pulse duration and ΔE the spectral bandwidth of the light pulse. The spectral brightness is an overall measure of the light source taking many factors into account such that it yields an estimate of the quality of the light source. The development of modern synchrotron light sources is hence often measured and compared to previous achieved values. Since all experiments are using X-rays of similar wavelength the big other factors are the number of photons and pulse duration. The more photons a source can create and the shorter the pulse duration the higher the spectral brightness. With this in mind, one can say the higher spectral brightness light sources are needed to image

Figure 2.1: Aerial view of the Linac Coherent Light Source (LCLS). LCLS uses the last third of the SLAC Linear Accelerator but is overall a 4.1km long machine. The accelerator and buildings are stretched far because of the process light is generated. Image from [1]

even smaller particles or look at dynamics that are even faster. Particular drivers for shorter pulse durations and higher intensities were the thoughts of visualizing electron movement at for example a chemical reaction but especially also the idea to study single particles. Another driver would be to study non-linear processes, for example absorption dynamics in atoms and molecules. One can conservatively estimate that a typical cross section at soft X-rays (1 nm wavelength) is around $\sigma = 1$ megabarn (Mb) [5], typical X-ray focii are round $A = 1\mu m^2$[1] such that the number of photons needed n_{in} to absorb just 1 photon per atom n_{abs} can be calculated by

$$n_{in} = \frac{n_{abs}A}{\sigma} = \frac{10^{-8}\text{cm}^2}{10^{-18}\text{cm}^2} = 10^{10} \tag{2.2}$$

While this back on the envelope type of calculation might be off by an order of magnitude or so depending on a the specific case, it illustrates that the amount of photons produced by modern synchrotron sources are not enough. An example of a modern synchrotron source is NSLS-II and a rough estimate yields that it produces roughly 1.710^4 photons per pulse in the Si111 bandwidth at pulse durations of a few ten picoseconds [6]. That is far out of reach to investigate non-linear processes. To reach the drastic higher number of photons per light pulse, it was proposed to build a laser in the XUV and later X-ray wavelength regime. Since, mirrors and lenses, optics as we know them, are not available in the short wavelength regime, one had to improvise. Instead amplifying light through an active medium by bouncing it back and forth between mirrors, one amplifies the

---

[1]Focus size at the AMO endstation at LCLS.
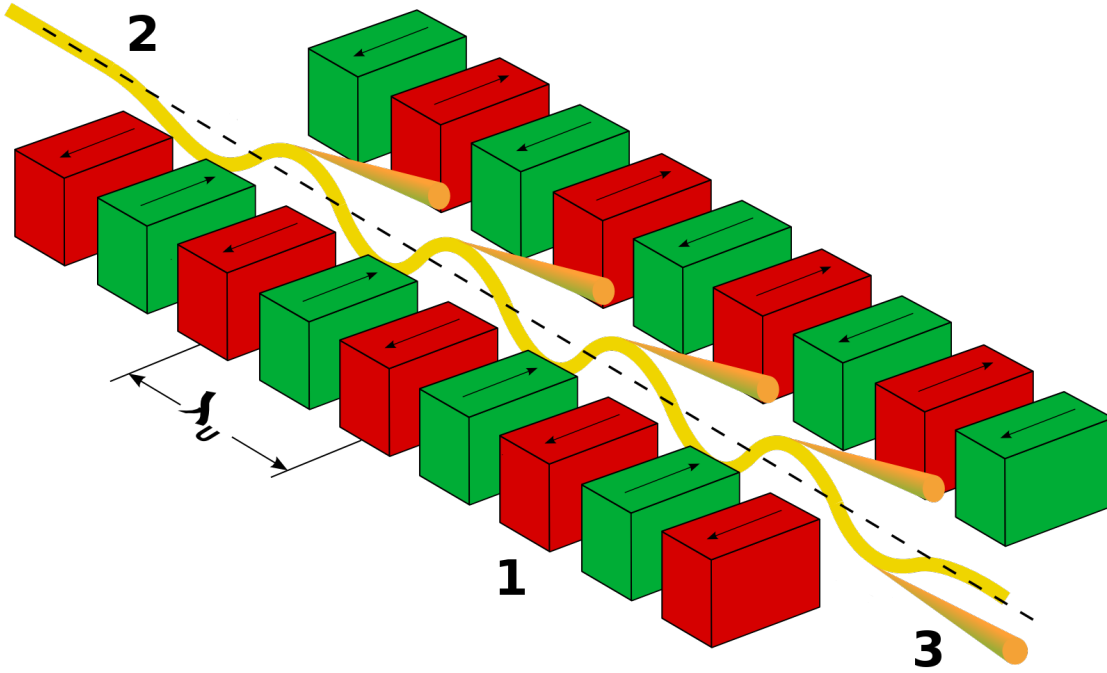
Figure 2.2: Schematic setup of an undulator with a period of λ_U. (1) Magnets in alternating polarity; the arrows indicate the direction of the magnetic field. (2) Incoming electron bunch near the speed of light. (3) Emitted light in beam direction due to sinusodial movement of the electron bunch. [2]

light along a straight line to create laser alike radiation[2] as it can be seen in the birds eye view of LCLS in figure 2.1. Ultimately, free-electron lasers were able to increase the number of photons per pulse to currently $n_{in} = 10^{12}$ and achieve pulse lengths of a few femtoseconds. These are remarkable beam parameters and as a result LCLS was increasing the spectral brightness by many orders of magnitudes.

2.1.1 Self amplification by spontaneous emission

In synchrotron lightsources as well as free electron lasers, X-rays are generated using wiggler and undulator magnets. In principle, an electron bunch is accelerated near the speed of light and then wiggled along its path using magnetic fields. The wiggling causes the particles to emit radiation. Wigglers consist of magnets that are arranged in an alternating order to force the electron bunch on a sinusodial trajectory. In a Wiggler, the electrons emit a total power $P_{emitted}$ that is proportional to the number of magnets

---

[2]The process to of the light create is explained in details in section 2.1.1.

m. CITE

$$P_{emitted} \propto m, \quad \text{in a wiggler magnet} \tag{2.3}$$

The emitted radiation has a braod, continuous spectrum and the center of that spectrum can be controlled by changing the speed or kinetic energy of the electron bunch. Wigglers have been used at the Stanford Synchrotron Radiation Lightsource (SSRL) in 1979 to generate X-rays and were a great success. Continued development on the Wiggler design led to the idea of Undulators. A schematic setup of an undulator magnet can be seen in figure 2.2. Wigglers and Undulators create radiation because of the same principle, an electron bunch is accelerated near the spead of light and then forced on a sinusodial pathway. In undulators, the separation of such magnets or undulator period λ_U and magnetic fields are chosen such that the emitted radiation per period constructively interferes with each other. The emitted wavelengths of undulators have a much more narrow pattern than thatof wigglers and because, strictly speaking, only one wavelength is amplified the emitted power P_W now scales with CITE

$$P_{emitted} \propto m^2, \quad \text{in an undulator magnet} \tag{2.4}$$

We can characterize an undulator by the undulator strength parameter K and it is given by [7]

$$K = \frac{e \ B \ \lambda_U}{2 \ \pi \ m_e \ c} \tag{2.5}$$

with the constants e being the electron charge, B being the magnetic field in the undulator, m_e being the mass of an electron and c being the speed of light, we can write

$$K \approx 9.34 10^{-3} B \ \lambda_U \ \text{T m} UNITCM? \tag{2.6}$$

Undulator magnets are large constructs of a few meters and their undulator period is on the order of centimeter. The electrons emit radiation in the nanometer wavelength regime because the electrons near the speed of light have to be considered relativistic and in the view of the electrons the undulator period λ_U appears shorter. We can correct for the relativistic effects and express the main amplified wavelength λ_r by CITE

$$\lambda_r = \frac{\lambda_U}{2\gamma} \left(1 + \frac{K}{2} + \gamma^2 \Psi^2 \right), \tag{2.7}$$

with the kinetic energy γ of the electron beam in the undulator and Ψ its observation angle. Equation 2.6 and 2.7 also show that the wavelength in an undulator is determined by the undulator gap λ_U, the magnetic field B in the undulator and the kinetic energy of the electron beam γ.

Undulators are also used in X-ray free electron lasers. The main difference to synchrotron radiation sources is that the light is amplified over a much longer straight line using multiple undulator magnets serially connected. LCLS has a 112m long undulator section. Over the course of this distance, microscopic effects start to play a role that could be neglected in typical synchrotron radiation sources. In vacuum, light will always be faster than electrons near the speed of light. This slight difference means that the copropagating photons and electrons have a phase difference and interact with each other. Depending on the phase, an electron will either gain or loose velocity. Over each undulator period, we can describe this *slip* with $\lambda_r(\Psi = 0)$. As a result, the initial unifrom electron density in the electron bunch is peridoically modulated and the modulated electron bunch structure is called *microbunching*. The creation of micobunching is illustrated in FIGURE. The increasingly structured electron beam amplifies a more narrow wavelength bandwidth and the number of electrons that are in phase with the photons increases over the travel length through the undulator. The electrons interact with the light field because of their narrow spatial and kinetic energy distributions. These parameters are characterized as the *emittance* of an electron bunch. Only the linear accelerator of a FEL are able to compress the electron bunch in space and energy, i.e. create a low emittance electron bunch, such that it can interact with the photons as described above. The initial process that starts this light amplification is triggered by the first few photons that are spontaneous emitted and then subsequently amplified. Hence, this type of radiation (or FEL operation mode) is called *Self Amplification by Spontaneous Emission* (SASE). It achieves laser alike amplification of the radiation power P_{SASE} that scales with the number of electrons N_e^2

$$P_{SASE} \propto N_e^2, \quad \text{SASE operation} \tag{2.8}$$

The characteristics of SASE radiation are its noisy and spiky photon spectrum, as seen in FIGURE, that come from the initial random (spontaneous) emission of photons.

X-ray free electron laser use one electron bunch and create one light pulse in a long set of undulator magnets, this is also called a *single-pass high-gain* FEL. Due to the lack of optics, X-ray FEL operate in the high-gain mode. A X-ray FEL gain curve as a function of gain length L_g can be seen in FIGURE. The electron bunch travels over a

long distance in the undulators until it eventually reaches saturation. In saturation, the microbunching is most developed. Since the creation of X-rays is affected by the kinetic energy of the electron bunch γ the electron bunch is not reused.

2.1.2 Soft X-ray self seeding

Free electron laser also have different operating modes than SASE. Particular interesting is the *seeded* type of operation, where the FEL amplifies an initial seed of photons. The photons seed can be created through various processes. Here again, the wavelength of the photon seed is the critical parameter in determining which method to choose. For example, in the infra red (IR) to extreme ultra violet (XUV) regime, conventional lasers can be used to place the initial photons seed. However, due to the lack of lasers available at soft and hard X-rays wavelength regimes, the idea of *self-seeding* gained traction. In self-seeding, an electron bunch is first send through a few undulator magnets to generate a few SASE phtons, the electrons and photons are then separated using a magnetic chicane, which also neutralizes the microbunching in the electron bunch. The monochromator selects a small wavelength slice from the comparably broad SASE spectrum of the inital photons. The photons exiting the monochromator are considered the *seed*. The seed and the electron bunch are overlapped again using the magnetic chicane and then send through more undulators. The seed generates now the microbuching, which is wavelength depended and thus a narrow wavelength band is amplified. Self-seeded beam operations have recently been demonstrated at LCLS. At hard X-rays, the Hard X-Ray Self-Seeding (HXRSS) instrument uses a diamond crystal to select a wavelength slice [8]. At soft X-rays, the Soft X-ray Self Seeding (SXRSS) instrument uses a grating as dispersive element [9]. A typical average spectrum of a soft X-ray self-seeded beam can be seen in Fig. **??**. The characteristics of this spectrum are an intense peak at the selected wavelength regime ontop of a broad SASE background. The background is an artefact of the amplification of some spontaeous emission events and can be suppressed by using fewer undulator magnets. Self-seeded beams have a significally reduced pulse energy by an order of magnitude or so, depending on the exact beam parameters, as compared to SASE operations. However, in their main peak, self-seeded beams have a higher spectral brightness when compared to a SASE spectrum. SASE spectra usually have a broad spectral bandwidth with a ΔE of a few eV, comparing seeded beams with Eq. 2.1 to SASE beams the increase in spectral brightness using seeded beams is understandable. The peak intensity in a narrow spectral band makes seeded beams interesting for a variety of applications particular in condensed matter physics, where it is instrumental to excite with narrow bandwidth photons. Of course there are also applications in atomic

and molecular physics, ranging from linear absorption spectroscopy on molecules that has been demonstrated recently [**?**], to non linear stimulated Raman spectroscopy [10], to ultrafast photoemission studies. Particular interesting for this work is the magnetic chicane from the SXRSS instrument that has been used as described in the next chapter.

2.1.3 Novel X-ray pump–probe techniques

In order to study X-ray induced methods using X-ray imaging and spectroscopy techniques, as it is discussed in the present work, two X-ray pulses are needed . Here, a pump pulse is used to induce dynamics in the sample system and a probe pulse is used to probe them at a certain time delay Δt. Pump–probe experiments are commonly used as they allow a precise study of dynamics. The pump pulse gives a very controllable starting point, i.e. time zero in the dynamic process, and the probe pulse can perform a measurement at a later time delay Δt. Sometimes pump and probe pulse are switched, which is indicated by a negative time delay Δt, often to verify time zero or to probe the system before any dynamics have occurred.

Creating two X-ray flashes to create a pump–probe experiment is a technical challenge and again this challenge is due to the lack of optics and the availability and size of X-ray SASE sources. In order to overcome this challenge, two methods have been proposed. Method one, mirror based beam-split and delay systems [11, 12] that split one pulse into a pump and probe beam and allow the delay of the latter. These systems typically are limited to short delay times, as the optics have to fit into existing setups and have a low transmission of X-rays over the mirrors. Method two, uses accelerator based schemes [3, 13] that manipulate electron bunches to create two X-ray pulses. Limitations arise depending on the scheme, e.g. limited pulse delay Δt or pulse energy split through limited electron beam separation or length of magnetic chicane. Both methods have been demonstrated at LCLS and have found use to complement the more widely available optical laser pump– X-ray probe methods particularly in the chemical sciences [14–16]. As the accelerator based X-ray pump – X-ray probe method using a magnetic chicane has been used, let us describe these schemes in greater detail. Before we jump into the technical details, it is good to know that not only the aspect of creating a time delay Δt between the pump and the probe pulse is important but also to create a difference in wavelength between these two pulses. Generally, this is of use to resonantly pump and off-resonance probe or vice versa. Equation (2.7) indicates which parameters can be tuned to create two pulses of different color. One, the undulator parameter K can be tuned to change the emitted wavelength, or two, the lorentz factor γ can be different if there are two electron bunches. The undulator period λ_U is fixed at LCLS.
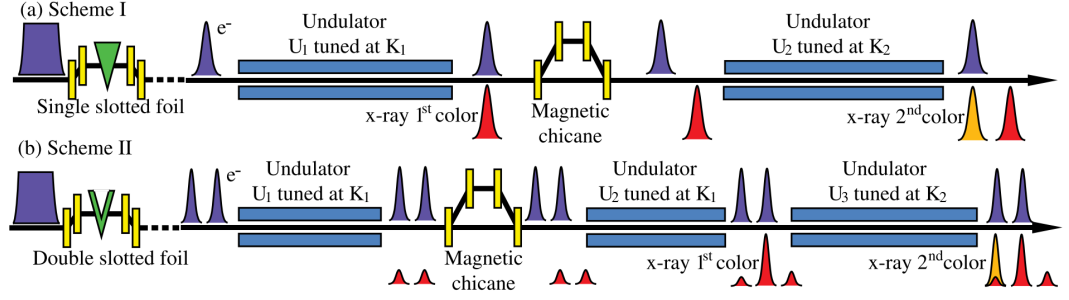
Figure 2.3: Schematic setup at LCLS of undulator parameter K_i based pump–probe schemes. Scheme I creates one electron bunch using a single slotted foil and scheme II creates two electron bunches using a double slotted foil. The electron bunches emit radiation with a wavelength depending on K_i. A time delay Δt between pulses is introduced using a magnetic chicane. Figure from [3] reprinted with permission from APS.

Undulator parameters $K_{1,2}$ based pump–probe scheme

The first developed accelerator based pump–probe technique at LCLS [3] uses a difference in undulator parameters $K_{1,2}$ to create two pulses of different wavelength, the time delay is introduced through a magnetic chicane and a schematic setup can be found in Figure 2.3.

In scheme I, one electron bunch is created through a single slotted foil[3] The use of the slotted foil enables control over the pulse duration. The electron bunch then travels through an undulator section U_1 tuned at strength parameter K_1 and is stimulated to lase but the process does not go into saturation to be able to reuse the electron bunch in the second undulator section. The time delay Δt between the two pulses is introduced by a magnetic chicane. At LCLS, a dedicated chicane, e.g. from the soft X-ray self-seeding instrument, can reach up to

$$\Delta t_{max} = 800 fs. \tag{2.9}$$

The minimal time delay can be achieved by setting the deflection in the magnetic chicane to zero in which case

$$\Delta t_{min} = \frac{l}{v_{el\ drift}} - \frac{l}{c} \approx 0 fs, \tag{2.10}$$

---

[3]A single slotted foil or emittance-spoiling foil works comparable to a monochromator. It leaves a certain energy band of the electron bunch within the slot unspoiled and Coulomb scatters or spoils (compare to apertures) the rest. The 'dispersive' element is a magnetic chicane. By narrowing the electron beam one also reduces its pulse duration [17].

with $l \approx 4m$ being the length between undulator sections U_1 and U_2 and c being the speed of light and $v_{el\ drift}$ being the drift velocity of the electron bunch. As the electron bunch travels close to the speed of light t_{min} is typically on the tens of attosecond timescale. The timing jitter between the two light pulses using only one electron bunch comes solely from the magnetic chicane due to the magnetic field jitter and the electron beam energy jitter. The total contribution to the timing jitter is less than 0.4% of the tim delay Δt imposed by the chicane. Since the delay chicane does not contribute significantly to the delay Δt a bigger factor is the velocity mismatch of the light pulse and the electron bunch. This mismatch can be estimated by

$$\Delta t_{beam\ mismatch} = \frac{N_u \lambda_r}{c}, \tag{2.11}$$

with N_u being the undulator periods. Given the parameters in study [3], $t_{beam\ mismatch} = 3fs$ such that a partial overlap could be achieved. However, the magnetic chicane removes the microbunching from section U_1. In undulator section U_2 tuned to undulator strength parameter K_2 the electron bunch lases again and the process is able to saturate. The maximal color separation between the two pulses is 1.9% in relative difference between K_1 and K_2.

Scheme II uses a double slotted foil[4] to create two electron beams. The two beams have a longitudinal separation that translates into the time delay Δt. The electron bunches travel through a first set of undulators U_1 that creates two pulses of the same wavelength, due to the shortness of the section U_1 the lasing process does not saturate. The electron bunches are then delayed using a magnetic chicane such that the leading electron bunch overlaps with the trailing light pulse. This light pulse now functions as a seed for the leading electron bunch such that this pulse saturates in undulator section U_2. The electron bunches then travel through the magnets at U_3, where the trailing electron bunch creates a second saturated pulse, the leading electron bunch barely emits radiation in U_3 since its energy spread has become too large after lasing in U_2. Using this method, two saturated lasing pulses can be generated, however, temporal overlap cannot be achieved.

Twin bunch or Lorentz factor γ based pump–probe scheme

The second developed accelerator-based pump-probe technique at LCLS [13] uses two electron bunches of different energy. A schematic setup of this beam operation can be found in figure 2.4.

---

[4]A double slotted foil works as a single slotted foil but it leaves to parts of the electron beam unspoiled through the two slots.
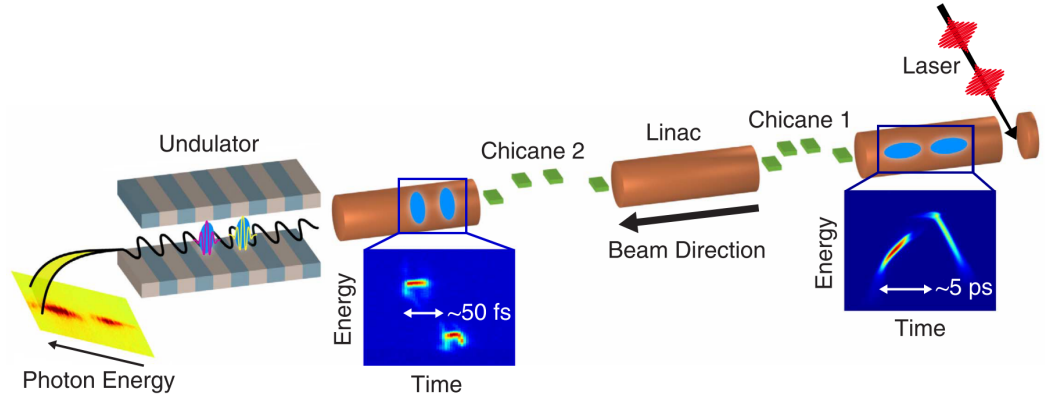
Figure 2.4: Schematic setup of the two bunch, two color pump–probe setup at LCLS. Two laser pulses shot at a cathode create two electron bunches with a delay Δt on the picosecond timescale. Two magnetic chicanes compress the bunches such that a delay Δt on the up to the ten femtosecond timescale is achieved. Both pulses go through one undulator section and the SASE lasing process is saturated. The relative color separation is on the order of 1%.

The bunches are created through a double laser pulse that impinges on a photocathode. Initially, these two bunches have a time delay of a few picoseconds, however, two magnetic chicanes compress the electron bunches in the time and intensity domain such that a time delay on the ten femtosecond timescale is achieved. The electron bunches then travel through one undulator section and both pulses saturate in their lasing process. At $8.3k$ eV, both pulses combined can reach pulse energies of $1.2mJ$, the color separation is 100 eV and the time separation ranges from $\Delta t_{min} = 0fs$ to $\Delta t_{max} = 100fs$. At hard X-rays, this method requires the pump pulse to have a higher photon energy than the probe pulse, although their respective intensities may vary. However, this method is not restricted to hard X-rays and can be utilized at soft X-rays. In the soft X-rays wavelength regime, where the above explained slotted spoiler foil can be used. This allows a further control to tune the time delay of the electron bunches, which enables scanning across each other.

2.2 Rare gas clusters

Rare gase clusters have been used as nanosample in this study and this chapter will explore this topic. Clusters have a long history to study light-matter interaction as their characteristics are well known [4]. Generally speaking, clusters are an aggregation

of atoms or molecules and vary in size. Their size can range from a few atoms to mesoscopic sizes such that one can classify a cluster as a bulk material. Clusters can form exotic materials that are interesting to study and can be well simulated through comparably simple computer models. Besides these testbed characteristics, the use of clusters has often practical purposes. They can be comparably easily generated and are typically easily tune able in size. Rare gas clusters are a subclass of clusters and they are bound by van der Waals forces and normally neutral-charged. Single van der Waals cluster typically form in an icosahedral[5] shape when they are sufficiently small (up to nanometer sized) [18] and have mostly a fcc-crystal[6] structure but exhibit also hcp-crystal[7] structures [19, 20]. The creation of homogenous and heterogeneous rare gas clusters shall be the focus of the next few chapters.

2.2.1 Creation of a homogenous cluster

Rare gas clusters, for example xenon clusters, can be generated through a variety of ways. While there are many ways to explain the cluster formation process, a kinetic model [21] gives a very intuitive way in the microscopic processes. In this kinetic model, atoms and clusters grow through collisions. We can express these collisions mathematically through the following reaction formula

$$A_n + A \rightleftharpoons A_{n+1}^*, \quad n = 1, 2, ..., \quad \text{monomer collision}, \tag{2.12}$$
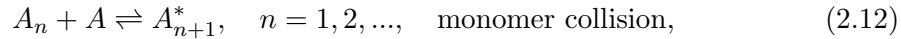
where a body A_n collides with a monomer A and form a metastable state A_{n+1}^* that will dissociate if not a subsequent collision deactivates it

$$A_{n+1}^* + M \rightleftharpoons A_{n+1} + M, \quad \text{activation/deactivation}. \tag{2.13}$$
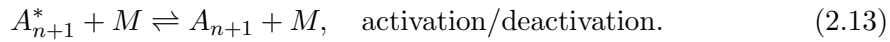
M is a chaperone that can be any kind of third body that removes energy from the system. Note that a chaperone M can also activate the state again. The binding force behind rare-gas clusters is the Van der Waals force, hence they are called Van der Waals cluster sometimes.

While the early stage of the cluster growth is driven by the monomer addition, cluster-cluster coagulation start to dominate the later growth processes [22, 23]. This is due to the quantitative increase in small clusters in the generation process that then start to collide, similar to above kinetic model. From empirical evidence, we know that clusters

---

[5]An icosahedron is a polyhedron with 20 faces, i.e. a dice with 20 faces.
[6]fcc is short for face-centered cubic. A very common crystal structure.
[7]hcp stands for hexagonal close-packed and is also a crystal structure.
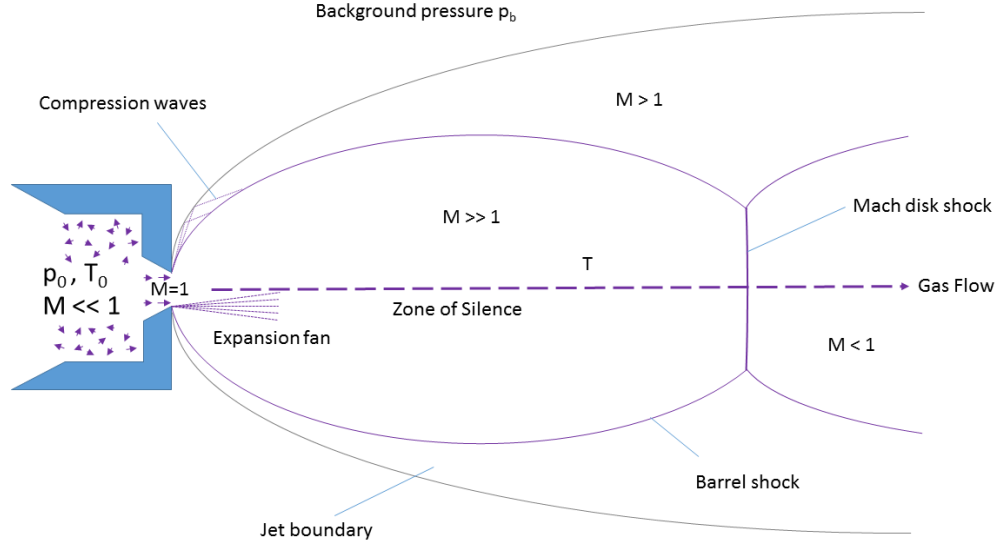
Figure 2.5: caption

solely generated through monomer addition have a size distribution of an exponential decay, whereas larger clusters that grew through coagulation follow a log-normal distribution. So through coagulation, the density of smaller clusters (and monomers and dimers) decreases through to cluster-cluster coagulation and larger clusters are formed. The most probable size of a cluster, i.e. the maximum of the log-normal distribution, is given by the parameters of the supersonic jet setup, which is what we will discuss next.

Supersonic jet setups typically store gas in a reservoir at a certain stagnation pressure p_0 and temperature T_0. The gas expands through a nozzle into a vacuum and figure 2.5 shows a schematic drawing of this process. Typical values for p_0 are 10 bars, where the mean free path of the atoms is much smaller than the nozzle diameter D. This is why many collisions occur during the expansion in the nozzle and the above described kinetic theory explains the cluster formation. However, this holds not true in the supersonic molecular flow region, where no further cluster growth happens. To understand the expansion process in detail, we assume to work with an ideal gas and to describe the gas expansion itself, we further assume that no clusters are formed and that turbulence and effects of heat conduction are unimportant [4, 24].

To begin, the velocity distribution of the gas follows a Maxwell-Boltzman distribution

with a mean velocity $\bar{v}$ that we can write down as

$$\bar{v} = \sqrt{\frac{2k_BT_0}{m_{gas}}}, \tag{2.14}$$

with the Boltzman constant k_B and the atomic mass of the gas m_{gas}. The movement direction of each atom is randomly orientated. Let us also define the enthalpy H_0 in the stagnation chamber

$$H_0 = c_pT_0, \tag{2.15}$$

with the specific heat c_p for atoms

$$c_p = \frac{5}{2}k_B, \tag{2.16}$$

The expansion of the gas through the nozzle is driven by the pressure difference p_{vac}/p_0. In the nozzle, the (steady) gas flow becomes directed and the enthalpy H_0 is converted into kinetic energy $\frac{1}{2}mv^2$ and a rest enthalpy H. So, in the expansion process, we can use the conservation of energy, and equation (2.16) we can write down

$$H_0 = H + \frac{1}{2}m_{gas}v^2 = c_pT + \frac{1}{2}m_{gas}v^2, \tag{2.17}$$

with T being the local temperature along the gas flow. To look at this in greater detail, let us define the Mach number M as the ration of the stream velocity v and the local speed of sound c_s

$$c_s = \sqrt{\frac{\gamma k_BT}{m_{gas}}}. \tag{2.18}$$

With the ratio of specific heats $\gamma = \frac{c_p}{c_v}$ at constant pressure and volume, they can be regarded as independent of temperature for atomic gases, we can rearrange equation 2.17 to

$$T = T_0\left(1 + \frac{1}{2}(\gamma - 1)M^2\right)^{-1}. \tag{2.19}$$

Here the interplay between the Mach number M^2 and the local temperature T give insight into the directed mass flow versus the remaining thermal energy in the system. As indicated the the figure 2.5, M increases dramatically along the expansion axis and that is due to decrease in speed of sound c_s that is proportional to $\sqrt{T}$ as indicated in equation (2.18). Finally, this attribute has given the name to supersonic jets.

Let us describe the appearance of the jet stream (see figure 2.5)next. Upon exiting the nozzle, the Mach number increases by a wide margin ($M >> 1$), that means that the gas travels faster than information in this medium. Here, a *zone of silence* is formed, where the gas flow is not influenced by other particles, thus uninterrupted. As the supersonic flow is exiting the nozzle it has to turn around the edge of the nozzle to further expand and the supersonic flow turns by actually creating smaller Mach waves. At the borders of the *zone of silence*, M decreases drastically resulting in dense regions that are called *barrel shock* to the sides and *Mach disk* downstream the gas flow. For an unhindered transport of the gas and clusters to the interaction region, the interaction region needs to be within the *zone of silence*. We can express the distance from the nozzle to the Mach disk through

$$\frac{x_{MD}}{d} = 0.67 \left(\frac{p_0}{p_b} \right)^{\frac{1}{2}}. \tag{2.20}$$

So the the competing stagnation pressure p_0 and the background pressure p_b define the distance of the otherwise static parameters. Hence, p_b needs to be low enough do drive the Mach disk downstream of the interaction region. By using skimmers and physically separating the jet expansion into separately pumped compartments, the background pressure p_b can be reduced.

While we have described a cooling gas in the expansion process it should be noted that the clusters are comparably hot. Through the kinetic process described above, they are efficiently heated. The two processes to loose energy are, one, collisions with a chaperone M that deactivates the cluster, or two, evaporation of monomers from the cluster. The evaporation process makes the temperature size-independent, after the clusters have reached a certain minimum size [25]. It is tedious and experimentally difficult to measure the temperature exactly but typically, the jet reaches temperatures of a few Kelvin and the cluster temperature is heavily dependent on their material, particular the dissociation energy. For this study relevant are mostly the temperature of Xenon cluster that is $75K$[8] and the fact xenon clusters are solid because their melting temperature is higher[26]. Follwing this same line of argumentation, helium clusters are liquid, which is why they are often called (helium-)droplets. If helium droplets are produced using a cryogenic jet even superfluid helium-droplets can be observed.

  At the current point of the discussion, it should shine out that the average cluster size is very much depended on the gas type, stagnation temperature T_0, stagnation pressure

---

[8]To put this temperature in perspective, krypton clusters are $50K$ and argon cluster $40K$ [25, 26]. Note that in this study the cluster size was $\bar{N} > 800$, hence above the minum value to be size independent. For the evaporative cooling process to settle at a given temperature, a certain flight distance (in the cited study 6.5cm) should also be taken into account.

Helium	Neon	Argon	Krypton	Xenon
3.85	185	1646	2980	5554

Table 2.1: Parameter K values for rare gases [**?**].

p_0 and the nozzle type. Indeed, an empirically found scaling law named after Hagena [**?**], can be written down as

$$\Gamma^* = KT_0^{0.25q-1.5}p_0 d_{eq}^q, \tag{2.21}$$

with the gas specific parameter K that can be found in table **??** for some rare gases, the gas specific parameter q that varies between 0.5 and 1 and is 0.85 for all rare-gases, and the equivalent nozzle opening d_{eq} that is $d_{eq} = d$ for pinhole sources and for conical nozzles d_{eq} reads

$$d_{eq} = d\frac{\tan{(\Phi_0)}}{\tan{(\Phi)}} \tag{2.22}$$

with the half opening angle of the nozzle Φ and the half opening of the free gas expansion Φ_0. The Hagena scaling parameter Γ^* allows us to estimate the mean cluster size, i.e. amount of accumulated particles per cluster $< N >$, as follows

- $\Gamma^* < 350$, no cluster formation observed.

- $350 < \Gamma^* < 1800$, in this region $< N >$ reads

$$< N >= 38.4 \left(\frac{\Gamma^*}{1000}\right)^{1.64} \tag{2.23}$$

- $1800 < \Gamma^*$, in this region $< N >$ reads

$$< N >= 33.0 \left(\frac{\Gamma^*}{1000}\right)^{2.35} \tag{2.24}$$

Supersonic jets generally create clusters of different sizes. This size distribution is centered around $< N >$ and for solid rare gas clusters, this distribution is a log-normal distribution. The size distribution can be an experimental challenge, especially when size dependent effects are investigated. Free electron laser allow the determination of the size of a single cluster through a diffraction image and by measuring enough single clusters, one can reproduce size distributions as in figure **??**. Historically, electron diffraction [**?**] and interferometric approaches [**?**] have been used to determine the size of clusters.

Experiments using supersonic jets for cluster generation are typically performed with
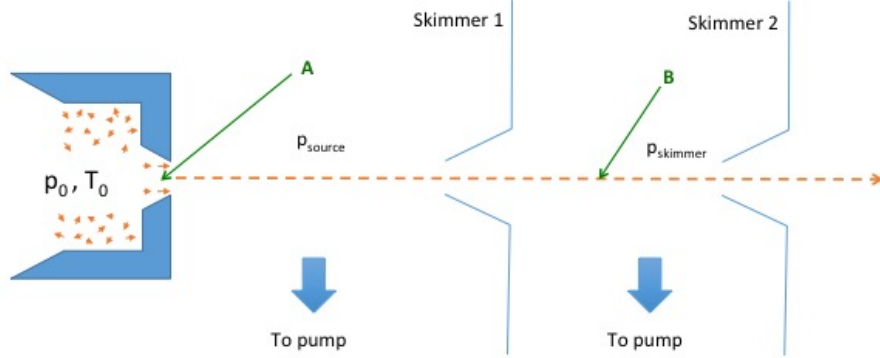
Figure 2.6: caption. After [4].

pulsed valves to decrease cost and gas load in the overall system. Upon opening and closing of the valve, the gas density varies. This mostly affects the cluster size and one would expect to see smaller clusters. This remains true in the beginning of the pulse but in the *afterpulse* one finds giant clusters that exceed the above described scaling laws [27].

2.2.2 Creation of a heterogeneous cluster

The creation of heterogeneous clusters as they have been used in this study stands in the foreground of this chapter. One of the possibilities to create heterogeneous clusters is through the principle of picing-up atoms or molecules [4]. Figure 2.6 illustrates pickup regions that are typically used in an experiment. Mainly, there are two different pickup processes, one, monomers are added to the cluster in region A of figure 2.6 that represents the nozzle of a supersonic source, or two, they can be picked up by a cluster in region B for example through an increase background pressure p_{b2}. If clusters pick up atoms or molecules in the nozzle region A, they can become part of the cluster formation and can be found inside of solid clusters. If atoms or molecules are picked up in region B, they stick to the surface of solid clusters but because the incoming cluster is so much larger and heavier than the colliding monomer the trajectory is not affected significantly.

The collision does add energy to the cluster, which is why it will loose particles through evaporative cooling again. The loss of particles through evaporative cooling is proportional to the ratio in dissociation energies of the cluster and picked up material. Already pressures of 10^{-11} bars over a pickup length of a few centimeters can dope the cluster in significant form. At these low pressures, picking up atoms or molecules in region B requires less gas load on the system but is also less efficient than picking up in region B. To increase the pickup levels in region B, a gas cell can be used as much higher pressures can be achieved within the gas cell without putting too much load on the overall system.

2.3 Introduction into X-ray scattering

2.3.1 Small angle X-ray scattering

- Switch to Guiniers approximation and description
- Work towards small angle scattering of small particles
- Particular spheres
- Discuss extreme positions

2.3.2 X-ray diffraction

- I wonder if I should include this to talk about 'what happens on faster timescales' using Ken's work.

2.3.3 The inverse problem: Phase retrieval

- Introduce some aspects from phase retrieval algorithms.

2.4 Light-matter interaction

2.4.1 Ionization of matter

2.4.2 Charge migration

2.5 Ionization of matter in intense X-ray pulses

- Short introduction coming from inelastic scattering

2.5.1 Formation of nanoplasma

- Step by step explanation on the formation of a nanoplasma

2.5.2 Tampered layers to inhibit the nanoplasma expansion

- Step by step explanation on the formation of the nanoplasma, pointing out the differences between tampered and pristine clusters.

3 Experimental Setup

3.1 The atomic, molecular and optcal physics instrument at LCLS

- Specifics to AMO
- For example focus studies and KBOs
- Use JSR and previous AMO articles

3.2 The LAMP end-station at AMO

- Specifics to the LAMP setup
- Use Journal of Synch. Radiation LAMP paper
- I think this can be a longer subsection since a lot of my work went into this.

3.3 The large area pn-CCD detectors

- Reuse our work on the LAMp-pnCCD paper
- I think this should be a longer chapter since a lot of my work has gone into this.

3.4 Time of flight mass-spectrometer

- fundamental aspects to the TOF detector
- I'm hoping on some specific drawings from Timur / LCLS and SIMION simulations from Timur here.

3.5 Sample delivery

4 Methods

4.1 The computing environment at LCLS

- Include basics around the PSANA interface
- For example how the date is converted, then stored and
- the analysis opportunities along the way - I think this will be a longer subsection since a lot of my work went into this and I'm regularly contacted about it. - Short introduction what we have to go through
- Reminder of detectors and analysis environment

4.1.1 PSANA - Python interaction with LCLS computing

4.2 pnCCD photon detectors

- Describe signal on the pnCCDs
- Calibrations and corrections - use LAMP paper
- single hits
- multiple hits

4.2.1 Signal analysis

- Present data from 1500eV photon energy on Xe backfilled chamber with the pnCCDs in spectroscopy mode to argue that the pedestal and offset corrections are enough to correct for fluoresence.
- Masked areas in image

4.3 Combining multiple pnCCD detectors

- Explain how I combined pnCCD detectors to perform reconstructions on it.
- Can reuse material from the LAMP pnCCD paper

4.4 Hitfinding

- Discuss the hitfinding.
- iTOF vs. pnCCD
- vs. Actual dynamics visible in diffraction images

4.5 Phase retrieval from a single diffraction pattern

- Short intro into phase retrieval

4.5.1 Solving the inverse problem

4.5.2 2D reconstructions and limitations

Hawk program

- Describe Filipe's program

Resolution enhancement through combination of rear and front pnCCD

- Showcase difference of rear pnCCD only vs. front + rear pnCCD vs. front + rear pnCCD 'cropped' for best results. Recycle work from LAMP pnCCD paper

4.5.3 1D reconstructions

- Describe my algorithm in 1D in detail

4.6 Summary of methods

- Comprehensive summary

5 Results and discussion

- Introduction of what we are looking for, reminder of hypothesis

5.1 Static data

5.2 Pristine xenon pump–probe data

- Presentation of Xe data

5.2.1 iToF traces with xenon as sample

- Xe iToF dynamics
- Slightly more of Xe higher charge-states present at longer delays.

5.2.2 Xenon diffraction images

- Present study of 1D condensed diffraction images.
- Work out similarities to Tais radiation damage

5.2.3 Reconstructions of xenon cluster single shot images

- Present Xe - cluster reconstructions
- Show 1D reconstructions and 'damage process'

5.2.4 pnCCD image pump – probe considerations

- Considerations of pump and probe pulse in one pnCCD image.

5.2.5 Time of flight data

5.3 Pristine helium cluster pump-probe data

- Presentation of He data

5.3.1 iToF data with helium as sample

- Subsection for iToF data, important to compare to HeXe data.

5.3.2 Diffraction images of helium cluster

- Work out radiation damage in 1D diffraction images.
- Introduce envelope to show the radiation damage effect - important to compare to HeXe data.
- Eventually subsection for reconstructions.

5.4 Helium-xenon core-shell systems and pump–probe data

-Presentation of HeXe data

5.4.1 Time-of-flight data of helium-xenon core-shell systems

- Show dynamics of XeHe data in tof trace.
- More hefty nanoplasma expansion in HeXe than in raw He.
- Complement with simulations from Phay.

5.4.2 Diffraction images of helium-xenon core shell systems

- Discuss diffraction images
- Show how scattering intensity drops from He signal but not from Xe signal.
- Eventually subsection for reconstructions.

5.4.3 Core-shell system considerations

5.5 Conclusion of the X-ray pump – X-ray probe study

- Conclusion where the results are compared to each other
- This experiment shows that heterogeneous clusters, as in tampered layers, do inhibit radiation damage of the sample target while the sacrificial layer undergoes a rapid nanoplasma transition.

6 Summary and outlook

6.1 Summary

Summary here

6.2 Outlook

Outlook here

Bibliography

[1] SLAC National Accelerator Laboratory. Lcls aerial overlay, 2009. URL `https://www.flickr.com/photos/slaclab/8577624017/`. Downloaded from SLAC's Flickr.

[2] Bastian Holst and Arpad Horvath. Undulator, Jul 2005. URL `https://commons.wikimedia.org/wiki/file:undulator.png`.

[3] A. A. Lutman, R. Coffee, Y. Ding, Z. Huang, J. Krzywinski, T. Maxwell, M. Messerschmidt, and H. D. Nuhn. Experimental demonstration of femtosecond two-color x-ray free-electron lasers. *Phys. Rev. Lett.*, 110(13):134801, 2013. ISSN 0031-9007.

[4] H Haberland. *Clusters of atoms and Molecules I, vol. 52 of Springer Series in Chemical Physics*. Springer-Verlag, Berlin, 1994.

[5] Philip H. Bucksbaum, Ryan Coffee, and Nora Berrah. *Chapter 5 - The First Atomic and Molecular Experiments at the Linac Coherent Light Source X-Ray Free Electron Laser*, volume Volume 60, pages 239–289. Academic Press, 2011. ISBN 1049-250X. doi: http://dx.doi.org/10.1016/B978-0-12-385508-4.00005-X. URL `http://www.sciencedirect.com/science/article/pii/B978012385508400005X`.

[6] G J Williams. personal communication, 2016.

[7] Zhirong Huang and Kwang-Je Kim. Review of x-ray free-electron laser theory. *Phys. Rev. ST Accel. Beams*, 10:034801, Mar 2007. doi: 10.1103/PhysRevSTAB.10.034801. URL `http://link.aps.org/doi/10.1103/PhysRevSTAB.10.034801`.

[8] J. Amann, W. Berg, V. Blank, F. J. Decker, Y. Ding, P. Emma, Y. Feng, J. Frisch, D. Fritz, J. Hastings, et al. Demonstration of self-seeding in a hard-x-ray free-electron laser. *Nat. Photonics*, 6(10):693–698, 2012. ISSN 1749-4885. doi: 10.1038/NPHOTON.2012.180. URL `http://www.nature.com/nphoton/journal/v6/n10/pdf/nphoton.2012.180.pdf`.

Bibliography

[9] D. Ratner, R. Abela, J. Amann, C. Behrens, D. Bohler, G. Bouchard, C. Bostedt, M. Boyes, K. Chow, D. Cocco, F. J. Decker, Y. Ding, C. Eckman, P. Emma, D. Fairley, Y. Feng, C. Field, U. Flechsig, G. Gassner, J. Hastings, P. Heimann, Z. Huang, N. Kelez, J. Krzywinski, H. Loos, A. Lutman, A. Marinelli, G. Marcus, T. Maxwell, P. Montanez, S. Moeller, D. Morton, H. D. Nuhn, N. Rodes, W. Schlotter, S. Serkez, T. Stevens, J. Turner, D. Walz, J. Welch, and J. Wu. Experimental demonstration of a soft x-ray self-seeded free-electron laser. *Phys. Rev. Lett.*, 114:054801, Feb 2015. doi: 10.1103/PhysRevLett.114.054801. URL `http://link.aps.org/doi/10.1103/PhysRevLett.114.054801`.

[10] Victor Kimberg, Alvaro Sanchez-Gonzalez, Laurent Mercadier, Clemens Weninger, Alberto Lutman, Daniel Ratner, Ryan N Coffee, Maximilian Bucher, Melanie Mucke, Marcus Agaker, Conny Sathe, Christoph Bostedt, Joseph Nordgren, Jan-Erik Rubensson, and Nina Rohringer. Stimulated x-ray raman scattering - a critical assessment of the building block of nonlinear x-ray spectroscopy. *Faraday Discuss.*, pages –, 2016. doi: 10.1039/C6FD00103C. URL `http://dx.doi.org/10.1039/C6FD00103C`.

[11] J. C. Castagna, B. Murphy, J. Bozek, and N. Berrah. X-ray split and delay system for soft x-rays at lcls. *J. Phys.: Conf. Ser.*, 425(15):152021, 2013. ISSN 1742-6596. doi: 10.1088/1742-6596/425/15/152021. URL `http://iopscience.iop.org/1742-6596/425/15/152021`.

[12] Brendan F. Murphy, Jean-Charles Castagna, John D. Bozek, and Nora Berrah. Mirror-based soft x-ray split-and-delay system for femtosecond pump-probe experiments at lcls. volume 8504, pages 850409–850409–7, 2012. doi: 10.1117/12.928538. URL `http://dx.doi.org/10.1117/12.928538`.

[13] A Marinelli, D Ratner, AA Lutman, J Turner, J Welch, F-J Decker, H Loos, C Behrens, S Gilevich, AA Miahnahri, et al. High-intensity double-pulse x-ray free-electron laser. *Nature communications*, 6, 2015.

[14] A. Picón, C. S. Lehmann, C. Bostedt, A. Rudenko, A. Marinelli, T. Osipov, D. Rolles, N. Berrah, C. Bomme, M. Bucher, G. Doumy, B. Erk, K. R. Ferguson, T. Gorkhover, P. J. Ho, E. P. Kanter, B. Krässig, J Krzywinski, A A Lutman, A M March, D Moonshiram, D Ray, L Young, S T Pratt, and S. H. Southworth. Hetero-site-specific X-ray pump-probe spectroscopy for femtosecond intramolecular dynamics. *Nature Communications*, 7(May):11652, 2016. ISSN 2041-1723. doi: 10.1038/ncomms11652. URL `http://www.nature.com/doifinder/10.1038/ncomms11652`.

B

[15] Ken R. Ferguson, Maximilian Bucher, Tais Gorkhover, Sébastien Boutet, Hironobu Fukuzawa, Jason E. Koglin, Yoshiaki Kumagai, Alberto Lutman, Agostino Marinelli, Marc Messerschmidt, Kiyonobu Nagaya, Jim Turner, Kiyoshi Ueda, Garth J. Williams, Philip H. Bucksbaum, and Christoph Bostedt. Transient lattice contraction in the solid-to-plasma transition. *Science Advances*, 2(1), 2016. doi: 10.1126/sciadv.1500837. URL `http://advances.sciencemag.org/content/2/1/e1500837`.

[16] Chelsea E Liekhus-Schmaltz, Ian Tenney, Timur Osipov, Alvaro Sanchez-Gonzalez, Nora Berrah, Rebecca Boll, Cedric Bomme, Christoph Bostedt, John D Bozek, Sebastian Carron, Ryan Coffee, Julien Devin, Benjamin Erk, Ken R Ferguson, Robert W Field, Lutz Foucar, Leszek J Frasinski, James M Glownia, Markus Gühr, Andrei Kamalov, Jacek Krzywinski, Heng Li, Jonathan P Marangos, Todd J Martinez, Brian K McFarland, Shungo Miyabe, Brendan Murphy, Adi Natan, Daniel Rolles, Artem Rudenko, Marco Siano, Emma R Simpson, Limor Spector, Michele Swiggers, Daniel Walke, Song Wang, Thorsten Weber, Philip H Bucksbaum, and Vladimir S Petrovic. Ultrafast isomerization initiated by X-ray core ionization. *Nature communications*, 6:8199, 2015. ISSN 2041-1723. doi: 10.1038/ncomms9199. URL `http://www.ncbi.nlm.nih.gov/pubmed/26354002`.

[17] P. Emma, K. Bane, M. Cornacchia, Z. Huang, H. Schlarb, G. Stupakov, and D. Walz. Femtosecond and subfemtosecond x-ray pulses from a self-amplified spontaneous-emission–based free-electron laser. *Phys. Rev. Lett.*, 92(7):074801, 2004.

[18] W Miehle, O Kandler, T Leisner, and O Echt. Mass spectrometric evidence for icosahedral structure in large rare gas clusters: Ar, kr, xe. *The Journal of chemical physics*, 91(10):5940–5952, 1989.

[19] B W Vandewaal. Icosahedral, decahedral, fcc, and defect-fcc structural models for Ar-N clusters, n>=500 - how plausible are they? *J Chem Phys*, 98(6):4909–4919, 1993. ISSN 00219606. doi: 10.1063/1.464946.

[20] Nina V. Krainyukova. 'The crystal structure problem' in noble gas nanoclusters. *Thin Solid Films*, 515(4):1658–1663, 2006. ISSN 00406090. doi: 10.1016/j.tsf.2006.05.041.

[21] D. Lippmann, W. C. Schieve, and C. Canestaro. Clustering time dependence in molecular dynamics: A kinetic model. *The Journal of Chemical Physics*, 81(11):

Bibliography

4969, 1984. ISSN 00219606. doi: 10.1063/1.447481. URL `http://link.aip.org/link/JCPSA6/v81/i11/p4969/s1{&}Agg=doi`.

[22] W.H. Zurek and W.C. Shieve. Multistep Clustering and Nucleation. *Journal of Physical Chemistry*, 84(12):1479–1482, 1980. ISSN 0022-3654. doi: 10.1021/j100449a010.

[23] J. M. Soler, N. García, O. Echt, K. Sattler, and E. Recknagel. Microcluster growth: Transition from successive monomer addition to coagulation. *Phys. Rev. Lett.*, 49: 1857–1860, Dec 1982. doi: 10.1103/PhysRevLett.49.1857. URL `http://link.aps.org/doi/10.1103/PhysRevLett.49.1857`.

[24] I Yamada. *Materials processing by gas cluster ion beams*, volume 34. 2001. ISBN 0927-796X. doi: 10.1016/S0927-796X(01)00034-1. URL `http://www.sciencedirect.com/science/article/pii/S0927796X01000341`.

[25] J. Farges, M. F. de Feraudy, B. Raoult, and G. Torchet. Structure and temperature of rare gas clusters in a supersonic expansion. *Surface Science*, 106(1-3):95–100, 1981. ISSN 00396028. doi: 10.1016/0039-6028(81)90186-2.

[26] J Gspann. *On the Phase of Metal Clusters*, pages 43–45. Springer Berlin Heidelberg, Berlin, Heidelberg, 1986. ISBN 978-3-642-71571-6. doi: 10.1007/978-3-642-71571-6_7. URL `http://dx.doi.org/10.1007/978-3-642-71571-6{_}7`.

[27] Daniela Rupp, Marcus Adolph, Leonie Fl??ckiger, Tais Gorkhover, Jan Philippe Müller, Maria Müller, Mario Sauppe, David Wolter, Sebastian Schorb, Rolf Treusch, Christoph Bostedt, and Thomas Möller. Generation and structure of extremely large clusters in pulsed jets. *Journal of Chemical Physics*, 141(4), 2014. ISSN 00219606. doi: 10.1063/1.4890323. URL `http://dx.doi.org/10.1063/1.4890323`.

D

7 Appendix

7.1 Python code on spherical integrations

7.2 Python code on combining detectors

E

8 Acknowledgment

This has to be written.